PHYSICAL REVIEW A **77**, 032905 (2008)

Scaling laws for guiding of highly charged ions through nanocapillaries in an insulating polymer

N. Stolterfoht, R. Hellhammer, J. Bundesmann, and D. Fink
Hahn-Meitner-Institut Berlin GmbH, Glienickerstrasse 100, D-14109 Berlin, Germany

(Received 16 January 2008; published 20 March 2008)

Guided transmission of highly charged ions through nanocapillaries in insulating PET polymers was investigated. Samples with highly parallel capillaries were used to study the ion guiding with a variety of ionic species, such as Ne^{7+}, Ne^{9+}, Ar^{9+}, Ar^{13+}, and Xe^{25+}. The incident energy was varied within the range of 3 −40 keV. The fraction of transmitted ions was measured as a function of the capillary tilt angle. The results are used to evaluate the guiding angle, which is a measure of the guiding power specifying the ability of a material to guide ions. Moreover, the angular profile of the transmitted ions was studied as a function of their energy and charge state. The profile width and the guiding angle were found to follow the same scaling law indicating that they are both determined by the main charge patch in the entrance region of the capillary.

DOI: 10.1103/PhysRevA.77.032905 PACS number(s): 61.85.+p, 34.50.Fa

I. INTRODUCTION

Recent studies from our laboratory [1–6] reported on ion transmission through capillaries in insulating polyethylene terephthalate (PET) polymers. When the capillary axis is tilted with respect to the incident beam direction, the transmission of highly charged ions in insulators was found to occur with negligible electron capture. In contrast to the work with metals [7–9], a considerable fraction of ions is guided through the capillary in its incident charge state. Due to the increasing interest in this subject, several laboratories started investigations of capillary guiding using PET [10–12], SiO_2 [13], and Al_2O_3 [14–16]. Moreover, electrons were used as projectiles guided through capillaries in Al_2O_3 [17] and PET [18]. The capillary work created lively and sometimes controversial discussions.

To understand the guiding phenomena, it was proposed that the incident ions deposit positive charge at the inner wall of the capillaries in a self-organizing process [1] as depicted in Fig. 1. For a tilted foil the deposited charge in the entrance region increases until the electrostatic field is sufficiently high for a deflection of the ions toward the direction of the capillary exit. Then, the charge deposition reduces to an amount sufficient to maintain the field for the ion deflection to the exit. As shown recently [19] an increase of the incident current does not change the charge patch in the entrance region, since the additional current flows away along the surface to the Au evaporated at the foil surface. This provides evidence that the discharge of the entrance patch is governed by a strongly nonlinear law.

Monte Carlo simulations [20,21] have explicitly shown that most of the deposited charge is located near the entrance region. Additional weaker patches may temporarily be produced after the first patch (Fig. 1). Finally, at equilibrium, the electric field within the inner part of the capillary plays a minor role, since an infinite homogeneously charged tube is field free (similarly as in a Faraday cage). Nevertheless, due to the loss of symmetry at the end of the capillary an electric field is produced by the charges deposited within the capillary. Thus, in the exit region, the ions are defocused leading to an widening of the transmission profile. Since the major charges are concentrated in the entrance region, it was recently suggested [5,21] that the entrance charge patch plays a significant role in forming the electric field at the capillary exit. However, it appears that this specific role of the entrance patch is not commonly accepted by the community concerned with capillary studies.

The capability of insulating capillaries to guide ions is referred to as the guiding power [22,23]. The fraction $f(\psi)$ of transmitted ions at equilibrium generally decreases with tilt angle ψ. The guiding power can be quantized by the guiding angle ψ_c for which the normalized transmission fraction drops as $f(\psi_c)/f(0)=1/e$. This definition of the guiding angle has been motivated by the observation that the tilt-angle dependence of the transmitted fraction can well be described by a Gaussian function [3,5]. It appears that the guiding angle depends on the material of the capillary samples and its surface treatment [13,15,19]. In particular, the guiding angle is governed by the ability of the material to store charges in the entrance patch. Moreover, if the guiding angle and the corresponding width of the transmission profile are produced by the same charge patch, a relationship between these angles is expected [22,23].

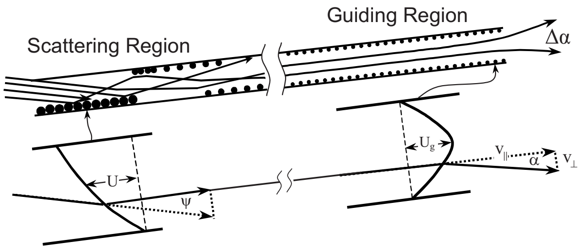

FIG. 1. Capillary guiding of ions in an insulating capillary. In the entrance region the main charge patch is created that deflects the ions to the capillary exit. The quantity U is a characteristic potential across the capillary diameter and ψ is the tilt angle. The exit region is affected by a symmetric potential of depth U_t in which the ions can gain perpendicular velocity $v_\perp$. The deflection angle α is obtained from $\tan\alpha=v_\perp/v_\parallel$, where $v_\parallel$ is the longitudinal velocity of the ion. Both potentials U and U_t are likely be produced by the dominant charge in the entrance patch.

In the present work, we performed systematic measurements with a variety of highly charged ions guided through PET capillaries. Preliminary results of the present studies have been published elsewhere [22,23,25]. We fabricated highly parallel capillaries by etching tracks of fast krypton ions, for which the angular spread of the ion tracks is negligible. The angular profiles of the transmitted ions were analyzed with respect to their width and intensity. The results are used to determine profile widths and guiding angles for various energies and charge states of the projectile. The profile width and the guiding angle are found to be governed by the same scaling law. With the observation of a linear relationship between these angles, we provide decisive experimental evidence that both angles are associated with the main charge patch located in the capillary entrance region.

II. BASIC FORMALISM

The potentials expected in the entrance and exit region are schematically drawn in Fig. 1. For the entrance region, we performed estimates of the potential using different charge distributions in the entrance patch. The calculation revealed a rather general form of the potential, which is not much affected by the charge distribution in the entrance patch. The potential drops quasilinearly in the transverse direction along the capillary diameter and in the longitudinal direction it has a maximum value near the center of the charge patch. Hence, the incident ion experiences different transverse fields as it travels along the entrance charge patch. Moreover, the transverse fields change with the trajectory of the ion, which enters the capillary in a statistical manner.

Similar effects influence the ions in the exit region. However, there, the field is radially symmetric with respect to the capillary axis [21]. Therefore, the deflection of the ions is also radially symmetric giving rise to the Gaussian like profiles observed in this work. Recently, in two-dimensional measurements, nearly circular transmission profiles have been observed [11,19]. Thus, the ions in the exit region experience different transverse fields when leaving the capillary. Again, the strength of the transverse field depends on the trajectory of the ion so that statistical effects are introduced into the scattering of the emerging ions.

We note the similarity of the ion deflections in the entrance and exit region. The potential in the exit region is symmetric in contrast to the potential in the entrance region. Nevertheless, one half of the exit potential is quite similar to that in the entrance region. Therefore, it appears reasonable that the formal treatments of the ion scatterings should be similar in the two regions.

In the following, we study the angular distribution of transmitted ions referred to as transmission profile. It represents the doubly differential ion yield $dY(\theta,\phi)/d\Omega$, where θ and ϕ are angles defined relative to the incident beam as angular deviations in the horizontal and vertical directions, respectively. Previous model calculations [3,5] have shown that the angular distribution of the transmitted ions may be described by the semi-empirical expression

$$\frac{dY(\theta,\phi)}{d\Omega} = \frac{dY_{\max}}{d\Omega}\exp\left(-\frac{E_p}{qU_t}\sin^2\alpha\right), \tag{1}$$

where E_p and q are projectile energy and charge, respectively, and $dY_{\max}/d\Omega$ is the maximum yield for $\alpha=0$. The ion emission angle $\alpha=\psi-\theta$ is measured relative to the capillary axis. The tilt angle ψ of the capillary sample is defined between the capillary axis and the beam direction (Fig. 1).

The effective potential U_t, which is a free model parameter, is responsible for the ion defocusing in the exit region of the capillary. In fact, the potential U_t is a characteristic value of a varying potential seen by the projectile during its emergence from the capillary (Fig. 1). In this potential an ion may gain the perpendicular energy $E_\perp=qU_t$. Then, the emission angle α is obtained from $\sin\alpha=v_\perp/v_\parallel=(qU_t/E_p)^{1/2}$, where $v_\perp$ and $v_\parallel$ are velocities perpendicular and parallel to the capillary axis, respectively. (Generally, the angles are sufficiently small so that $\sin\alpha\approx\alpha$.)

To interpret the semiempirical expression (1) we note that it is similar to the well-known Boltzmann law, which involves a distribution of kinetic energies and a single thermal energy parameter. Here, in Eq. (1), the value qU_t characteristic for the distribution of potential energies is related to the single kinetic energy $E_\perp=E_p\sin^2\alpha$.

Next, we consider the total yield of the transmitted ions obtained by integration over the angles θ and ϕ

$$Y(\psi)=\int\frac{dY(\theta,\phi)}{d\Omega}d\Omega. \tag{2}$$

This quantity can be converted to the fraction of transmitted ions

$$f(\psi)=\frac{Y(\psi)}{Y_{in}}, \tag{3}$$

i.e., the number ratio of transmitted to incident ions in a given capillary.

Similarly to the transmission profile, the fraction of transmitted ions can be described by [2,3]

$$f(\psi)=f_0\exp\left(-\frac{E_p}{qU}\sin^2\psi\right), \tag{4}$$

where $f_0\lesssim 1$ is the transmitted fraction at $\psi=0$. The free model parameter U is an effective potential difference across the capillary diameter produced by the charge deposited in the entrance region (Fig. 1).

Equation (4) is based on the assumption that the ions are lost by deposition at the capillary wall if the perpendicular energy $E_\perp=E_p\sin^2\psi$ exceeds the deflection energy qU. We note that Eq. (4) is again similar to the Boltzmann law. Hence, from Eqs. (1) and (4) we keep in mind that the transmission profile and the fraction of transmitted ions are governed by expressions, which are equal apart from the different potentials U and U_t.

III. EXPERIMENTAL METHOD

The measurements were performed at the 14.5 GHz Electron Cyclotron Resonance (ECR) source of the Ionenstrahllabor (ISL) at the Hahn Meitner Institute in Berlin using the ultrahigh vacuum chamber shown in Fig. 2 [1,3]. The chamber is operated with a base pressure of 10^{-10} mbar. The target foils were mounted on a goniometer, which allowed for tilting the capillaries with high precision relative to the inci-

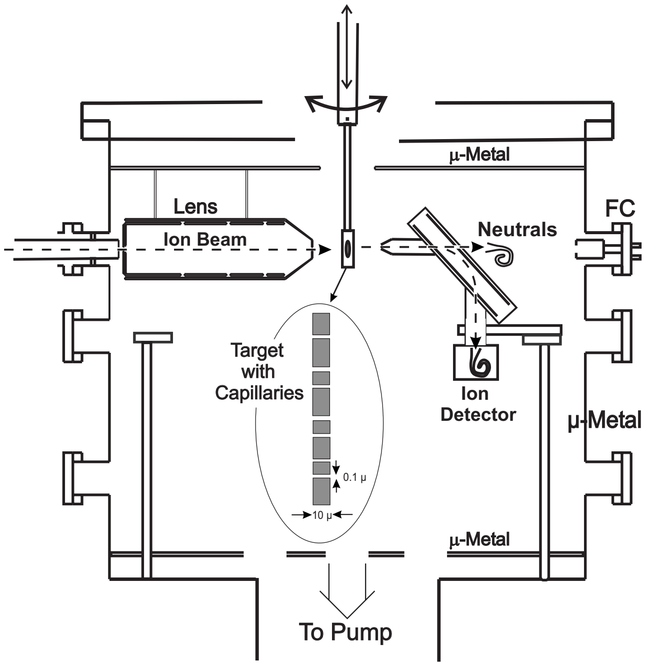

FIG. 2. Ultrahigh vacuum chamber built essentially by a μ metal. The ion beam is focused in a lens system and directed on the target sample containing capillaries. The transmitted ions are measured with an electrostatic analyzer, which is rotatable around the chamber axis.

dent beam. The ion beam was collimated to a diameter of 1.5 mm with a current of typically $0.1-1$ nA corresponding to a current density of $0.044–0.44$ nA/mm^2. The divergence of the beam was better than 0.3° full width at half maximum (FWHM). The ions were measured using an electrostatic analyzer whose angular resolution was 0.35° FWHM. The energy resolution was 5% which was sufficient to separate the charge states of the transmitted ions.

For the experiments, PET capillary samples were manufactured. The capillaries have a diameter of about 200 ± 20 nm and a length of 12 ± 1 μm. A description of the etching technique to produce capillaries in PET can be found elsewhere [26]. Optimal results with respect to straightness, aspect ratio, parallelism of the capillaries were obtained using 250 MeV krypton ions, for which the effect of Rutherford scattering is negligible [24]. The angular spread of the capillary inclination was estimated to be ~0.2° FWHM which significantly smaller than the aspect angle of 1°. Figure 3 shows a typical example for the surface of a PET foil, obtained by means of scanning electron microscopy (SEM). The capillary entrances are seen as black circles. The front and the back of the PET foil were evaporated under 45° with Au forming a film of ~20 nm thickness. We used foils with a capillary density of 10^8 cm^{-2}. This density implies a mean distance of ~1 μm between neighboring capillaries and a geometric opening of about ~3%.

The experimental results showed ion guiding in the PET capillaries in accordance with previous studies [1]. For Ne^{7+} impact parallel to the capillary axis the intensity of the transmitted ions in the initial charge state is found to be dominant, whereas the intensities of the other charge states, including neutrals, are smaller by about two orders of magnitude. This finding is consistent with previous measurements using capillaries in conducting materials [7,8]. However, the final charge-state distribution of the transmitted ions does not change much when the foil is tilted. Rather, it is found that the guided ions retain their incident charge during the passage through the capillaries. Since the incident charge state is dominant we shall exclusively consider this charge state in the following analysis.

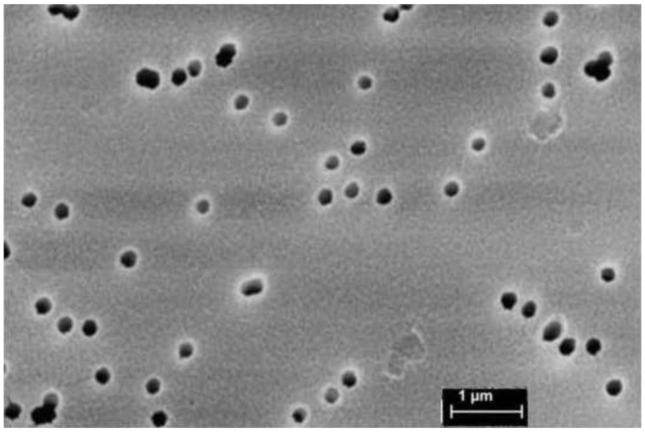

FIG. 3. Density plot showing capillaries with a diameter of ~200 nm and a density of 10^8 cm^{-2}. The foil surface is evaporated with a gold layer of 20 nm thickness. The graph was obtained by means of scanning electron microscopy.

IV. TRANSMISSION PROFILES

We first discuss results for Ne^{7+} ions, which have frequently been used in previous studies [1–3]. In Fig. 4 the transmitted Ne^{7+} ion intensity is plotted as a function of the observation angle θ (defined relative to the incident beam direction). Transmission profiles were measured for incident energies of 3, 5, 7, and 10 keV (Fig. 4). Data are obtained for an untilted foil with $\psi=0°$ and tilt angles within the range of $\psi=5-15°$. The transmission profile is normalized to the charge $Q_d=1$ nC deposited on the front surface of the PET foil (covered with Au). We note that the results are taken under equilibrium conditions, i.e., for sufficient charge accumulation with which the transmission profile does not change any more.

It is seen that the overall intensity of the transmission profiles decreases with increasing tilt angle. The decrease of the total intensity is governed by the guiding angle ψ_c at which the intensity of the transmission profile drops to the value of $1/e$. The guiding angle and the corresponding guiding power decrease with the incident energy. (More information about the guiding angle will be given after integration of the transmission profiles.) Moreover, Fig. 4 shows that the width of the transmission profile decreases with increasing energy. This behavior has also been observed in previous studies [6,11,21].

In Fig. 5 further examples of transmission profiles are plotted. The data are taken for 7 keV Ne^{7+}, 13 keV Ar^{13+},

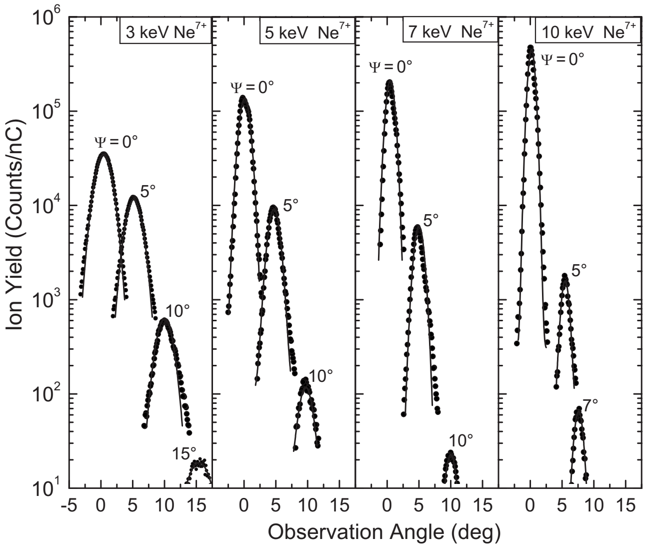

FIG. 4. Transmission profiles of Ne^{7+} ions measured for tilt angles ψ in the range of $0°-15°$. The incident energies are 3, 5, 7, and 10 keV as indicated in the graphs. The experimental data are fitted by Gaussian functions given as solid lines.

and 25 keV Xe^{25+}, i.e., for constant energy to charge ratio. The results are found to be nearly equal with respect to intensity and width of the transmission profiles. This finding indicates that the major parameter governing the transmission profile is the energy-to-charge ratio of the projectile. In particular, it appears that the guiding properties are independent of the projectile mass. This finding is interesting in view of the recent measurements using electrons [17,18].

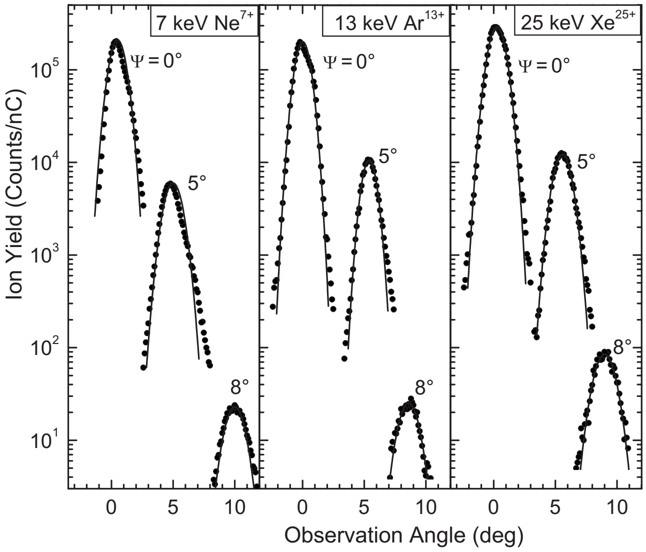

FIG. 5. Transmission profiles of 7 keV Ne^{7+}, 13 keV Ar^{13+}, and 25 keV Xe^{25+} measured for tilt angles ψ=0°, 5°, and 8°. Note the similarities of corresponding profiles obtained with a constant energy-to-charge ratio of the projectile. The experimental data are fitted by Gaussian functions given as solid lines.

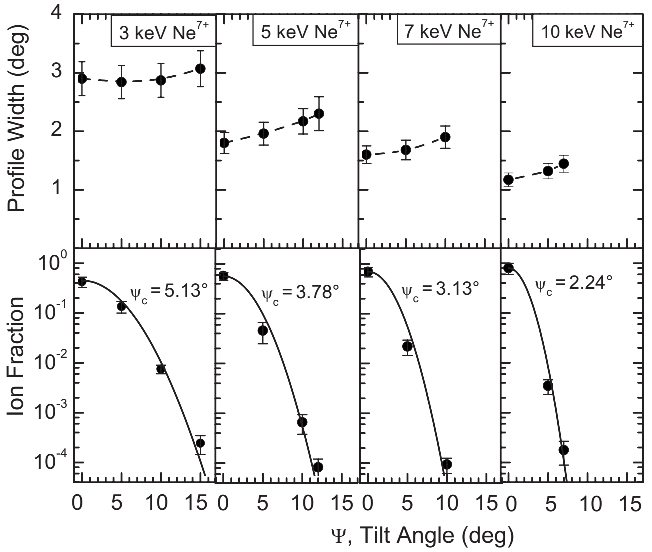

FIG. 6. Properties of the Ne^{7+} transmission profiles given in Fig. 4. The upper row shows the FWHM σ_t of the profiles and the lower row shows the fraction $f(\psi)$ of transmitted ions as a function of the tilt angle. The dashed lines (upper row) shall guide the eye and the solid lines (lower row) represent Gaussian fit functions. The guiding angle ψ_c, given at each graph in the lower row, characterizes the $1/e$ drop of the corresponding Gaussian function.

To analyze the experimental results we make use of Eq. (1) in accordance with previous observations [1–4] showing that a transmission profile can well be fitted by the Gaussian-like function

$$\frac{dY(\theta,\phi)}{d\Omega} = \frac{dY_{\max}}{d\Omega}\exp\left(-\frac{\sin^2\alpha}{\sin^2\alpha_t}\right). \tag{5}$$

The angle α_t represents the width of the Gaussian function, which is treated as an adjustable parameter when fitting the experimental data. As seen from Figs. 4 and 5 the measured transmission profiles agree well with the Gaussian fit function (5).

In previous studies it is common practice to use the full width at half maximum (FWHM) σ_t, which is obtained from $\sin \sigma_t = 2\sqrt{\ln 2}\, \sin \alpha_t$. In the upper row of Fig. 6 the fit results of the FWHM σ_t are given for Ne^{7+} impact. For 3 keV the width is found to be practically constant with varying tilt angle ψ. At higher energies the width increases somewhat with ψ. However, we note that the width variation barely exceeds the experimental uncertainties. The near independence of profile width on the tilt angle is a remarkable finding, which has already been noted in early studies of the capillary guiding [1].

Figure 6 indicates that the width of the transmission profiles decreases with increasing projectile energy. For 3 keV the width amounts to $\sigma_t \approx 2.8°$, which drops to 1.3° at 10 keV. Similar dependencies on the projectile energy have been found for the other ion species studied in the present work. Previous model calculations [2,3] suggest that the profile width σ_t is proportional to $(q/E_p)^{1/2}$. Indeed, a preliminary analysis appears to confirm this dependence. However, with the large variety of projectiles studied here, a more accurate

E_p/q dependence can be determined as will be shown in the section devoted to scaling laws.

V. TRANSMITTED ION FRACTIONS

Next, we determine the fraction of transmitted ions by integration of the transmission profiles. In the present experiments using an electrostatic spectrometer, the transmission profiles are measured at $\phi=0$ as a function of the observation angle θ (defined relative to the incident beam direction). Since only the single $\phi=0$ angle was measured, an extrapolation in the unobserved ϕ region was required.

This was done assuming that the profile in ϕ direction can be fitted by a Gaussian function as well as for the θ direction (Figs. 4 and 5). Hence, the integration of Eq. (2) can be performed analytically:

$$Y(\psi) = \frac{\pi}{4\ \ln 2}\frac{dY_{\max}}{d\Omega}\sigma_\theta\sigma_\phi, \tag{6}$$

where σ_θ and σ_ϕ are the FWHMs in θ and ϕ directions, respectively. Since in the experiments no information was available about σ_ϕ we have set $\sigma_\phi=\sigma_\theta=\sigma_t$ for simplicity. This assumption, which implies that the transmission profiles are circularly symmetric, may introduce systematic errors. Previous two-dimensional measurements of the transmitted ions [19] show typical deviations from the circular symmetry by ~20%. However, such deviations are within the uncertainties of the absolute yield of the transmitted ions.

The values of $dY_{\max}/d\Omega$ and σ_t, obtained from the profile fittings were used in Eq. (6) to determine the total yield $Y(\psi)$ which, in turn, was converted to the fraction $f(\psi)$ of transmitted ions by means of Eq. (3). In the lower row of Fig. 6 the transmitted fractions of Ne^{7+} ions are plotted a function of the tilt angle ψ. In Fig. 7 further examples are depicted for Ar^{13+} and X^{25+}. All graphs show that the fraction of transmitted ions decreases with the tilt angle.

We note that the Ne^{7+} ion fraction for the untilted foil ($\psi=0$) amounts to $f_0 \approx 0.45-0.8$ as the incident energy increases from 3–10 keV. These results indicate a relatively high transmission through the present capillaries at zero tilt angle. Similar results were found for the other ion species (Fig. 7). For nontilted straight capillaries, most of the ions are directly transmitted through the capillaries. We do not expect ion guiding since no significant charge patch is produced in the capillaries. Rather, we would expect that the ions traveling in the direction of the capillary wall are lost by deposition. Such losses originate from the divergence of the ion beam and the capillaries. In addition, the attraction by the image charge tends to increase the ion impact on the wall [9]. The image-charge effect is likely to be responsible for the observed increase of the ion loss with decreasing ion energy.

For the further analysis, we make use of Eq. (4) showing that the experimental fraction of transmitted ions can be fitted by the Gaussian-like function [3,5,17]

$$f(\psi) = f_0 \exp\left(-\frac{\sin^2\psi}{\sin^2\psi_c}\right). \tag{7}$$

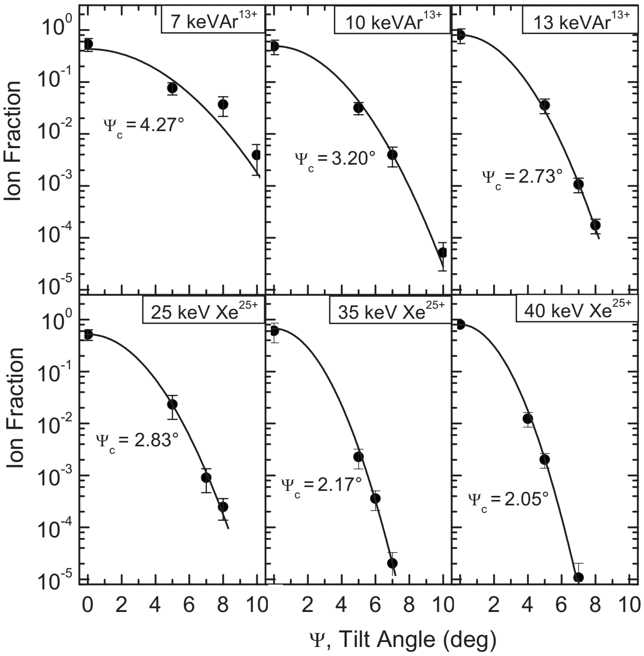

FIG. 7. Fraction $f(\psi)$ of transmitted ions derived from the transmission profiles partially given in Fig. 5. The upper and lower rows show the fraction $f(\psi)$ of transmitted Ar^{13+} and Xe^{25+} ions, respectively, as a function of the tilt angle. The solid lines represent Gaussian fit functions. The guiding angle ψ_c, given at each graph, characterizes the $1/e$ drop of the corresponding Gaussian function.

The fit procedure determines the characteristic tilt angle ψ_c referred to as guiding angle (which is a measure for the guiding power). It is pointed out, however, that ψ_c is defined without any model assumption, since it can experimentally be obtained as the angle for which $f(\psi_c)/f(0)=1/e$.

Figures 6 and 7 indicate that the Gaussian fits compare well with experimental data of the transmitted ion fraction. The guiding angles obtained from the fits are given in the graphs showing the transmitted ion fractions. In the following, the guiding angles will be further analyzed.

VI. SCALING LAWS

In this section, we summarize the complete set of results obtained for the profile width and the transmitted ion fraction and analyze them in terms of scaling laws. Experiments were performed using the ions Ne^{7+} and Ne^{9+} at 3–10 keV, Ar^{9+} and Ar^{13+} at 7–13 keV, and Xe^{25+} at 25–40 keV. As shown before, the results for the profile widths σ_t and the guiding angle ψ_c were determined by fit procedures.

Following the prediction of Eqs. (1) and (4), the experimental results for $\sin^{-2}\sigma_t$ and $\sin^{-2}\psi_c$ are plotted versus the energy-to-charge ratio E_p/q as shown in Figs. 8(a) and 8(b), respectively. Both data sets follow universal curves, which indicate that the angles σ_t and ψ_c scale with E_p/q. In the following, the attempt is made to determine the explicit E_p/q dependencies of σ_t and ψ_c.

From the comparison of Eqs. (1) and (5) it follows that

$$\sin^{-2}\sigma_t = \frac{1}{4\ \ln 2}\frac{E_p}{qU_t}. \tag{8}$$

With a constant U_t, this expression predicts a linear relation between $\sin^{-2}\sigma_t$ and E_p/q. Indeed, in Fig. 8(a) the experi-

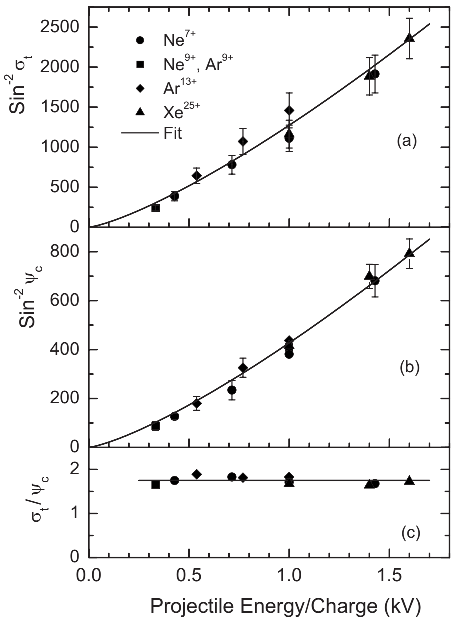

FIG. 8. Scaling laws for the width σ_t (FWHM) of the transmission profile and the guiding angle ψ_c. In (a) and (b) the quantities $\sin^{-2}\sigma_t$ and $\sin^{-2}\psi_c$, respectively, are plotted as a function of the energy-to-charge ratio E_p/q. In (c) the ratio ψ_c/σ_t is plotted showing its constancy within the experimental uncertainties. The solid lines represent fit functions discussed in the text.

mental data exhibit a near linear increase with the energy-to-charge ratio of the projectile.

However, there are deviations from the linear dependence, in particular, for small E_p/q values. Therefore, to improve agreement between the model calculations and the experimental data, we suggest a weak E_p/q dependence of the potential

$$U_t = \frac{Q_\infty}{c_t}\left(\frac{E_p}{q}\right)^{-0.3}, \tag{9}$$

where Q_∞ is the equilibrium charge deposited primarily in the entrance region and c_t is a constant similar to a capacity. Hence, Eq. (8) in conjunction with the potential U_t from Eq. (9) is used as a fit function where Q_∞/c_t is treated as an adjustable parameter. In Fig. 8(a) the results of the fit are shown as a solid line, which agrees well with the experimental data.

Similar to the previous treatment, we obtain from the comparison of Eq. (4) and Eq. (7)

$$\sin^{-2}\psi_c = \frac{E_p}{qU}. \tag{10}$$

Using this expression, the experimental data are fitted in conjunction with

$$U = \frac{Q_\infty}{c_e}\left(\frac{E_p}{q}\right)^{-0.3}, \tag{11}$$

where the constant c_e is associated with an effective capacity in the entrance region. In Fig. 8(b) again an excellent agreement is found between the experimental data and the fit function. We note that in the present analysis, both potentials U_t and U are assumed to be produced by the same equilibrium charge Q_∞ accumulated near the entrance of the capillary.

TABLE I. Potentials U and U_t characteristic for the entrance and the exit region, respectively, for some energy-to-charge ratios of the projectile.

E_p/q (kV)	0.43	1.0	1.5
U (V)	3.0	2.3	2.0
U_t (V)	0.36	0.29	0.25

Consequently, not only the general structure of the expressions (1) and (4) are the same but also the explicit E_p/q dependencies of the deflection potentials are equal. In Fig. 8(c) the equal dependencies are accurately confirmed by the constant ratio $\psi_c/\sigma_t = 1.75$. The only difference between the expressions (9) and (11) lies in the constants c_e and c_t, which determine the potentials U_t and U.

In Table I these potentials are given for a few values of E_p/q. It is seen that U_t and U slightly decrease with increasing energy-to-charge ratio, which follow from their $(E_p/q)^{-0.3}$ dependencies. A possible explanation of these (weak) dependencies may be due to the fact that at higher energies the ions penetrate into the capillary wall, wherein part of the deposited charge is screened. Thus, U and U_t are reduced with increasing E_p/q values, since both potentials are affected by the same screening of the charge in the entrance region.

From the data in Table I it follows that $U_t/U = 0.12$. (The same value follows for c_e/c_t). Hence, the potential U_t in the exit region is nearly an order of magnitude smaller than the potential U in the entrance region. This result seems plausible, since both potentials are presumably produced by the same charge patch in the entrance region. The exit potential is much farther away from the main charge patch than the entrance potential.

In fact, regarding the large aspect ratio of 60 for the present capillaries, we would expect that the value of U_t/U is smaller than 0.12. A reason for an enhancement of the exit potential might be the effect of adjacent capillaries [21]. It is likely that the charge patches in neighboring capillaries increase the field in the exit region, while they do not affect much the field in the corresponding entrance region. However, this increase is not expected for capillaries of low density. Recent measurements [5,19] performed with the relatively small capillary density of 4×10^6 cm^{-2} yielded transmission profiles with FWHMs ranging from 1°–3°. These latter results leave some open questions. We suggest that further work is needed to clarify the role of neighboring capillaries.

VII. DISCUSSION AND CONCLUSION

In the present analysis, the width σ_t of the transmission profiles and the corresponding guiding angle ψ_c were determined for various highly charged ions species. The angles were obtained from similar treatments based on the assumption that the transmission profile and the tilt-angle dependence of the transmitted fraction are described by Gaussian functions. This finding indicates that the processes for the deflection of the ions in the capillary entrance and exit region are similar. Moreover, the occurrence of the Gaussian functions suggests statistical processes involved in the ion deflection. Each deflection field in the entrance and exit region is spread within a certain range characterized by an effective potential. The actual potential, affecting the moving ion, depends on its trajectory which, in turn, is governed by statistical rules. Thus, the expressions in Eqs. (1) and (4) reveal similarities to the Boltzmann law.

An important issue of the present work is the search for scaling rules for the angles σ_t and ψ_c. We found that both angles can be scaled by the energy-to-charge ratio of the projectile. This is plausible since E_p/q is a well-known scaling parameter for ion trajectories governed by an electrostatic field. In addition to the scaling rules, we deduced the explicit E_p/q dependence for the angles σ_t and ψ_c. Both expressions $\sin^{-2}\sigma_t$ and $\sin^{-2}\psi_c$ are found to be nearly linearly dependent on E_p/q.

The remaining nonlinearity is likely created by a weak $(E_p/q)^{-0.3}$ dependence of the potentials U_t and U. This dependence may be produced by screening effects resulting in a reduction of the charge in the entrance patch. The observation of the constant ratio $\psi_c/\sigma_t = 1.75$ suggests that both potentials are affected by the same screening effect. This provides further experimental evidence that the potentials in the entrance and exit regions are produced by essentially the same charge near the entrance patch.

The conclusion that the exit potential is determined by the entrance patch appears counter intuitive, since it seems more likely that this potential is produced by charges transported to the capillary exit. It should be realized, however, that indications for this counterintuitive conclusion has already been provided in earlier studies. Based on experimental evidence, it was pointed out [5] that the exit width σ_t and its time evolution is nearly constant with increasing tilt angle, while the transport of charge to the capillary exit varies strongly (by orders of magnitude). Hence, it was alternatively suggested that the exit width is produced by the main charge patch near the entrance [5]. Similarly, in model calculations [21] it was postulated that the charge in the entrance patch is responsible for the exit potential.

However, from the model calculations [21] it was concluded that the broadening of the transmission profile cannot exceed the FWHM of ~1°. In view of the present experimental evidence, we conclude that the broadening of the transmission profile by the entrance charge patch can well be as large as 3°. Moreover, the profile width of ~5°, observed in the early capillary experiments [1], is likely produced by the charge accumulated in the entrance patch, since its guiding angle was found to be $\psi_c = 9°$. This value is rather high indicating that a relatively large amount of charge is accumulated in the entrance patch.

The observation that the width of the transmission profile is determined by the entrance charge patch allows for interesting verifications. For instance, the time evolution of the entrance charge $Q(t)$ can be determined from the temporal increase of the corresponding profile width. Moreover, information about the total charge Q_∞ in the entrance patch at equilibrium can be obtained. Since the width of the transmission profile is found to remain practically constant with varying tilt angle (Fig. 6) it may be concluded that the total charge accumulated in the entrance patch is rather constant.

This observation again appears counter intuitive, since the discharge of the entrance patch is expected to be governed by the density of the deposited charge which, in turn, is inversely proportional to the tilt angle. Obviously, the deposited charges move quickly apart [21] so that finally a constant charge density is achieved. In any case, the present model calculations are based on the assumption that the amount of accumulated charge Q_∞ is independent on the tilt angle. However, we suggest further work to gain information about the charge distribution in the entrance patch.

From the observed proportionality of ψ_c and σ_t it follows that the guiding angle increases monotonically with the charge in the entrance patch, as implemented in Eq. (10) together with Eq. (11). This monotonic increase implies that the guiding power is primarily governed by the ability of the capillary material to store charges in the entrance patch. However, we would not expect that the proportionality between ψ_c and σ_t holds for larger values of the entrance charge. For sufficiently large charge deposition, the ions are not directed to the exit of the capillary but to the capillary wall opposite to the entrance patch.

Hence, a secondary charge patch can be produced (Fig. 1). Evidence for such secondary or even tertiary charge patches have been found in the simulations of capillary guiding [20,21]. However, these additional charge patches are only transiently produced during the time evolution of the ion guiding. At equilibrium conditions the secondary patches lose significance. It appears that self-organizing mechanisms in conjunction with nonlinear effects [19] inhibit the overcharging of the entrance patch.

In view of the linear relationship between the angles ψ_c and σ_t, it is interesting to consider other capillaries of different aspect ratios and surface treatments. As mentioned, in the early experiments using 3 keV Ne^{7+} with 100 nm capillaries, the unusually large guiding angle of $\psi_c = 9°$ and the exit width of $\sigma_t = 5°$ have been achieved [1]. Similar as in the present work, the values of $\psi_c = 5.4°$ and $\sigma_t = 3°$ have been obtained for 3 keV Ne^{7+} guided through 200 nm capillaries with a density of $4\times10^6\ \mathrm{cm}^{-2}$ [19]. Moreover, 3.5 keV Ne^{7+} experiments performed with other PET samples of $4\times10^6\ \mathrm{cm}^{-2}$ yielded significantly smaller guiding and exit angles, i.e., $\psi_c = 3°$ and $\sigma_t = 1.3°$ [11]. These few examples show that the angles ψ_c and σ_t may vary significantly but their ratios are close to the value $\psi_c/\sigma_t \approx 1.75$ observed in this work. Hence, we would expect that the potentials U and U_t producing these angles, vary but their ratios are likely close to the present value of $U_t/U = 0.12$.

It would be instructive to verify the ψ_c/σ_t ratio for other materials, e.g., $\mathrm{SiO_2}$ [13] and $\mathrm{Al_2\ O_3}$ [15]. As noted in Ref. [13], $\mathrm{SiO_2}$ has a relatively large electrical conductivity, which may limit the charge collection in the entrance patch and, hence, may be responsible for the small guiding power and exit width observed. In future applications it would be favorable to find materials which optimize the need for a high guiding power and sharpness of the exit distribution. Also, future work is needed to improve the theoretical understanding of the capillary guiding. Previous simulations [20,21] still contain adjustable parameters and have imperfections since they are not capable to explain profile widths of 2°–5° observed in various laboratories [1,10,15,17,19]. It would be desirable to perform *ab initio* calculations that may serve as a milestone for further comparison with experiments.

ACKNOWLEDGMENTS

We are grateful for very stimulating discussions with Bela Sulik, John Tanis, and Yasuyuki Kanai. We thank P. Szimkowiak for preparing the PET capillaries.

[1] N. Stolterfoht, J. H. Bremer, V. Hoffmann, R. Hellhammer, D. Fink, A. Petrov, and B. Sulik, Phys. Rev. Lett. **88**, 133201 (2002).

[2] N. Stolterfoht, V. Hoffmann, R. Hellhammer, D. Fink, A. Petrov, Z. D. Pešić, and B. Sulik, Nucl. Instrum. Methods Phys. Res. B **203**, 246 (2003).

[3] N. Stolterfoht, R. Hellhammer, Z. D. Pešić, V. Hoffmann, J. Bundesmann, A. Petrov, D. Fink, and B. Sulik, Vacuum **73**, 31 (2004).

[4] N. Stolterfoht, R. Hellhammer, Z. D. Pešić, V. Hoffmann, J. Bundesmann, A. Petrov, D. Fink, B. Sulik, M. Shah, K. Dunn, J. Pedregosa, and R. W. McCullough, Nucl. Instrum. Methods Phys. Res. B **225**, 169 (2004).

[5] R. Hellhammer, P. Sobocinski, Z. D. Pešić, D. Fink, J. Bundesmann, B. Sulik, and N. Stolterfoht, Nucl. Instrum. Methods Phys. Res. B **232**, 235 (2005).

[6] R. Hellhammer, P. Sobocinski, Z. D. Pešić, D. Fink, J. Bundesmann, B. Sulik, and N. Stolterfoht, Nucl. Instrum. Methods Phys. Res. B **233**, 213 (2005).

[7] Y. Yamazaki, Phys. Scr. **T73**, 293 (1997).

[8] S. Ninomiya, Y. Yamazaki, F. Koike, H. Masuda, T. Azuma, K. Komaki, K. Kuroki, and M. Sekiguchi, Phys. Rev. Lett. **78**, 4557 (1997).

[9] K. Tökési, L. Wirtz, C. Lemell, and J. Burgdörfer, Phys. Rev. A **61**, 020901(R) (2000).

[10] G. Víkor, R. R. Kumar, Z. Pešić, N. Stolterfoht, and R. Schuch, Nucl. Instrum. Methods Phys. Res. B **233**, 218 (2005).

[11] Y. Kanai, M. Hoshino, T. Kambara, Y. Yamazaki, R. Hellhammer, and N. Stolterfoht, in *Proceedings of the XXIVth International Conference on Photonic, Electronic, and Atomic Collisions*, edited by F. D. Colaveccio *et al.* (University Press, Rosario, 2005), p. Fr131.

[12] M. Fürsatz, S. Pleschko, I. C. Gebeshuber, H. P. Winter, C. Lemell, N. Stolterfoht, and F. Aumayr, in *Proceedings of the XXIVth International Conference on Photonic, Electronic, and Atomic Collisions* (Ref. [11]), p. Fr132.

[13] M. B. Sahana, P. Skog, G. Víkor, R. T. Rajendra Kumar, and R. Schuch, Phys. Rev. A **73**, 040901(R) (2006).

[14] H. F. Krause, C. R. Vane, F. W. Meyer, H. M. Christen, and I. O. P. Publishing, J. Phys.: Conf. Ser. **58**, 323 (2007).

[15] S. Mátéfi-Tempfli, M. Mátéfi-Tempfli, L. Piraux, Z. Juhász, S. Biri, É. Fekete, I. Iván, F. Gáll, B. Sulik, G. Víkor, J. Pálinkás, and N. Stolterfoht, Nanotechnology **17**, 3915 (2006).

[16] P. Skog, I. L. Soroka, A. Johansson, and R. Schuch, Nucl. Instrum. Methods Phys. Res. B **258**, 145 (2007).

[17] A. R. Milosavljević, G. Víkor, Z. D. Pešić, P. Kolarž, D. Šević, B. P. Marinković, S. Mátéfi-Tempfli, M. Mátéfi-Tempfli, and L. Piraux, Phys. Rev. A **75**, 030901(R) (2007).

[18] S. Das, B. S. Dassanayake, M. Winkworth, J. L. Baran, N. Stolterfoht, and J. A. Tanis, Phys. Rev. A **76**, 042716 (2007).

[19] N. Stolterfoht, R. Hellhammer, J. Bundesmann, D. Fink, Y. Kanai, M. Hoshino, T. Kambara, T. Ikeda, and Y. Yamazaki, Phys. Rev. A **76**, 022712 (2007).

[20] K. Schiessl, W. Palfinger, C. Lemell, and J. Burgdörfer, Nucl. Instrum. Methods Phys. Res. B **232**, 228 (2005).

[21] K. Schiessl, W. Palfinger, K. Tökesi, H. Nowotny, C. Lemell, and J. Burgdörfer, Phys. Rev. A **72**, 062902 (2005).

[22] N. Stolterfoht, R. Hellhammer, J. Bundesmann, and D. Fink, Radiat. Eff. Defects Solids **162**, 515 (2007).

[23] R. Hellhammer, J. Bundesmann, D. Fink, and N. Stolterfoht, in *16th International Workshop on Inelastic Ion-Surface Collisions*, edited by F. Aumayr and C. Lemell, Hernstein, Austria, 2006, p. 53; R. Hellhammer, J. Bundesmann, D. Fink, and N. Stolterfoht, Nucl. Instrum. Methods Phys. Res. B **258**, 159 (2007).

[24] R. Hellhammer, P. Sobocinski, D. Fink, J. Bundesman, B. Sulik, and N. Stolterfoht, in *Proceedings of the XXIVth International Conference on Photonic, Electronic, and Atomic Collisions* (Ref. [11]), p. Tu129.

[25] R. Hellhammer, J. Bundesmann, D. Fink, and N. Stolterfoht, Nucl. Instrum. Methods Phys. Res. B **261**, 149 (2007).

[26] R. Spohr, *Ion Tracks and Microtechnology* (Viehweg, Braunschweig, 1990).